

This is an Open Access document downloaded from ORCA, Cardiff University's institutional repository: <https://orca.cardiff.ac.uk/id/eprint/177361/>

This is the author's version of a work that was submitted to / accepted for publication.

Citation for final published version:

Ekim, Utku, Ilter, Emre, Çelik, Harun Samet, Genc, Aziz, Slater, Thomas J.A. , Çelikkilek Ersundu, Miray and Ersundu, Ali Erçin 2025. Sm₂O₃-doped CsPbBr₃ perovskite quantum dot glass nanocomposites for enhanced plant growth lighting. *Materials Today Chemistry* 45 , 102624. 10.1016/j.mtchem.2025.102624

Publishers page: <http://dx.doi.org/10.1016/j.mtchem.2025.102624>

Please note:

Changes made as a result of publishing processes such as copy-editing, formatting and page numbers may not be reflected in this version. For the definitive version of this publication, please refer to the published source. You are advised to consult the publisher's version if you wish to cite this paper.

This version is being made available in accordance with publisher policies. See <http://orca.cf.ac.uk/policies.html> for usage policies. Copyright and moral rights for publications made available in ORCA are retained by the copyright holders.



Sm₂O₃-Doped CsPbBr₁I₂ Perovskite Quantum Dot Glass Nanocomposites for Enhanced Plant Growth Lighting

Utku Ekim ^a, Emre İltter ^a, Harun Samet Çelik ^a, Aziz Genç ^b, Thomas J. A. Slater ^b, Miray

Çelikkilek Ersundu ^{a*}, Ali Erçin Ersundu ^{a*}

^a Yildiz Technical University, Faculty of Chemical and Metallurgical Engineering, Department of Metallurgical and Materials Engineering, Glass Research and Development Laboratory, Istanbul, 34220, Turkey

^b Cardiff Catalysis Institute, School of Chemistry, Cardiff University, Cardiff, CF10 3AT UK

Abstract

Indoor farming systems have emerged as a vital solution to the growing challenges in agriculture, where light quality and intensity are crucial for enhancing photosynthesis and promoting plant growth. While LEDs are widely employed in these systems, thanks to their energy efficiency and tunable spectra, conventional phosphor-based LEDs often face limitations such as rapid degradation and suboptimal color rendering. To address these challenges, we synthesize Sm₂O₃-doped CsPbBr₁I₂ perovskite quantum dot (PQD) glass nanocomposites (GNCs), aiming to enhance red light emission for plant growth. The incorporation of Sm₂O₃ allows precise tuning of the emission spectrum, improving photoluminescence quantum yield (PLQY) to create an optimal light environment for plant development. Our systematic investigations identify the ideal Sm₂O₃ concentration and heat-treatment conditions, achieving a remarkable PLQY of 44.3%, the highest reported for CsPbBr_xI_(3-x) PQD GNCs. Through controlled melt-quenching and heat-treatment processes, we optimize the crystallization conditions, ensuring the stability and longevity of the PQDs within the glass matrix. Additionally, we construct a prototype plant growth LED panel by integrating 450 nm blue LED chips with the Sm₂O₃-doped CsPbBr₁I₂ PQD GNCs, achieving a total photosynthetic photon flux density (PPFD) of 240 $\mu\text{mol}\cdot\text{m}^{-2}\cdot\text{s}^{-1}$, a luminous efficacy of 171 lm/W,

and CIE color coordinates of $x = 0.3756$ and $y = 0.2575$. Plant growth experiments indicate that plants grown under our LED system demonstrate longer stems and larger leaves compared to those cultivated under standard white LEDs. The results indicate that Sm_2O_3 -doped $\text{CsPbBr}_1\text{I}_2$ PQD GNCs hold great promise for next-generation plant growth lighting, offering a novel and energy-efficient approach that could transform indoor agriculture and foster advancements in sustainable farming technologies.

Keywords: Perovskite quantum dots, plant growth LEDs, Sm_2O_3 doping, quantum yield, $\text{CsPbBr}_1\text{I}_2$ glass nanocomposites

*Corresponding authors—E-mail: miray@yildiz.edu.tr (Miray Çelikkbilek Ersundu), ersundu@yildiz.edu.tr (Ali Erçin Ersundu)

1. Introduction

Modern agricultural techniques offer innovative solutions to escalating challenges such as land depletion, soil degradation, water scarcity, and the unpredictability of climate change driven by urban expansion [1–3]. Among these techniques, indoor farming systems enable year-round crop production, independent of seasonal changes, by optimizing plant growth and yield through precise control of environmental conditions, including CO_2/O_2 levels, humidity, temperature, and most importantly, light intensity, quality, and daily light/shadow ratios [4–9].

Light, in particular, plays a pivotal role in photosynthetic efficiency, making it the most critical factor to optimize in indoor farming [8]. Although plants have evolved to utilize the full spectrum of sunlight, they are primarily adapted to absorb red and blue regions of visible light [9]. Specifically, red light is absorbed by phytochrome red pigments (P_r) to promote stem growth, while far-red light is used by phytochrome far-red pigments (P_{fr}) to facilitate germination and flowering. Additionally, chlorophyll a and b regulate photosynthesis by absorbing blue and red light, which fuels nutrient production essential to plant biology [8–10]. Current research shows that plants

require high-intensity red and blue light to synthesize nutrients, promote growth, and stimulate their cellular photoreceptors and pigments [11]. Thus, effective management of red and blue light in indoor plant cultivation has the potential to enhance productivity and support sustainable agricultural practices by optimizing nutrient synthesis and growth processes. This need has driven the popularity of indoor farming, where light intensity and wavelength can be precisely controlled. In this context, LEDs have become the preferred lighting solution, particularly due to their tunable spectra, along with their compact size, energy efficiency, low carbon footprint, and non-toxic nature [12,13].

The significant advancements in LED performance have largely resulted from the development of luminescent phosphor materials, which have undergone extensive research and refinement alongside LED chip technology [14]. Despite their widespread use, phosphor materials face challenges such as rapid degradation and poor color rendering over time, prompting continued research to improve their performance [15]. One promising strategy to address these challenges involves doping phosphor materials with transition metals or rare-earth ions, which enhances emission intensity, improves correlated color temperature and color rendering index, and enables more precise color tuning [16–18].

Blue light is typically sourced directly from LED chips, sometimes enhanced with Tm^{3+} ions to achieve greater purity and intensity, making it a well-established component [19,20]. The main focus, however, remains on delivering high-intensity, tunable red light [21,22]. Eu^{3+} , Sm^{3+} , and Mn^{4+} ions, alone or in combination, have been widely studied as red-light boosters [23–31]. Nevertheless, the narrow and sharp emission peaks of rare-earth ions at specific wavelengths present a significant limitation, as plants have evolved to utilize broader wavelength ranges rather than isolated peaks.

To address these limitations, perovskite quantum dots (PQDs), particularly CsPbX₃ (X = Cl, Br, I), have garnered significant attention for their remarkable optical properties and tunable emission spectra [32]. However, the intrinsic instability of PQDs under operational conditions has driven efforts to enhance their durability through encapsulation in robust matrices. Glass, in particular, has emerged as an optimal host material due to its exceptional mechanical, chemical, and thermal stability, integrating the superior emission characteristics of PQDs with the durability of glass [33]. Recent studies have explored the impact of glass matrix composition and microstructural regulation on the photoluminescence (PL) properties of PQDs [34]. For instance, the depolymerization of the glass network facilitates ion migration, nucleation, and grain growth of CsPbX₃ PQDs, leading to enhanced PL characteristics [35]. However, this approach may compromise the structural stability of the glass, adversely affecting the long-term stability of PQDs. Interestingly, rare-earth ions have demonstrated significant potential to enhance PQD crystallization within glass matrices by serving as effective nucleation sites [36]. Moreover, the striking overlap between the emission and absorption regions of PQDs and rare-earth ions suggests the possibility of energy transfer processes that could further enhance photoluminescence properties [37-39]. To date, several iodide-based PQD GNCs (e.g., CsPbI₃, CsPbBr_xI_{3-x}) have been developed to achieve pure and intense red emission [40-44]. Nevertheless, further tuning of red emission and performance optimization remain crucial for their application in plant growth LEDs [45]. Previous studies have shown that the energy levels of Sm³⁺ ions are well-matched with CsPbBr_xI_{3-x} PQDs, enhancing the PLQY and offering a promising approach for optimizing the red-light emission wavelength [46]. Additionally, Sm³⁺ ions can further refine this emission by aligning it with the optimal spectra for plant absorption, providing multiple peaks in this region [19].

Therefore, in this study, we synthesize CsPbBr₁I₂ PQD glass nanocomposites (GNCs) doped with varying concentrations of Sm₂O₃ to fine-tune the emission for enhanced plant growth, using the

conventional melt-quenching technique followed by controlled heat-treatment. We identify the crystallization conditions of PQDs through Sm_2O_3 doping and optimize the concentration to achieve the maximum PLQY value and the optimal emission spectrum for plant growth. Finally, we construct a prototype plant growth LED by coupling a 450 nm blue LED chip with a selected sample, achieving a remarkable PLQY of 44.3%. This demonstrates that Sm_2O_3 -doped $\text{CsPbBr}_1\text{I}_2$ PQD GNCs are promising candidates for next-generation plant growth lighting systems.

2. Experimental procedure

2.1 Synthesis of Sm_2O_3 -doped $\text{CsPbBr}_1\text{I}_2$ GNCs

Four different sets of $\text{CsPbBr}_1\text{I}_2$ PQD GNCs, doped with varying concentrations of Sm_2O_3 (hereafter referred to as $\text{PQD@GNC:Sm}_2\text{O}_3$), are synthesized using the conventional melt-quenching technique followed by a controlled heat-treatment process. The nominal glass compositions are $5\text{CaO}-10\text{ZnO}-2\text{Al}_2\text{O}_3-30\text{B}_2\text{O}_3-35\text{SiO}_2-(5\text{Cs}_2\text{O}-3\text{PbO}-3\text{NaBr}-6\text{NaI}) + x\text{Sm}_2\text{O}_3$ (where $x = 0, 1, 2,$ and 3 mol%). Raw materials, including CaCO_3 , ZnO , Al_2O_3 , H_3BO_3 , SiO_2 , Cs_2CO_3 , PbO , NaBr , NaI , and Sm_2O_3 , are sourced from Sigma-Aldrich and Alfa Aesar in analytical reagent grade (>99.9%) and are used without further purification. The materials are accurately weighed using high-precision scales (± 0.0001 g), mixed, and ground into a fine powder using an agate mortar and pestle. The resulting mixture is melted in alumina crucibles at 1100 °C for 30 minutes. The molten glass is then poured into preheated (400 °C) stainless-steel molds and annealed in a muffle furnace for 5 hours to relieve internal stresses induced during quenching. While minor compositional variations due to halide volatilization during melt-quenching cannot be entirely ruled out, our previous study demonstrates that the halide composition remains stable after the first melt-quenching cycle under similar processing conditions [47].

Heat-treatment is conducted at 590 °C, 600 °C, 610 °C, and 620 °C, each for a duration of 15 minutes. After heat-treatment, the samples are naturally cooled and polished to a thickness of 2.5

mm to achieve surfaces of high optical quality suitable for characterization. The synthesized samples are coded as $x\%Sm_2O_3-T^{\circ}C$, where $x\%$ represents the mol% of Sm_2O_3 dopant and T represents the heat-treatment temperature (e.g., $0\%Sm_2O_3-600^{\circ}C$ for the undoped sample heat-treated at $600^{\circ}C$, and $2\%Sm_2O_3-620^{\circ}C$ for the 2 mol% Sm_2O_3 -doped PQD GNC heat-treated at $620^{\circ}C$). Samples not subjected to the heat-treatment process are referred to as "as-cast" throughout this paper (e.g., $0\%Sm_2O_3$ -as-cast).

2.2 Characterization studies

The thermal properties of the as-cast samples are analyzed using a Netzsch Simultaneous Thermal Analyzer - STA 449 F3 Jupiter instrument, where a 25 ± 1 mg powdered sample is sealed in a platinum pan and heated at a rate of $10^{\circ}C/min$ under a constant flow of nitrogen gas. X-ray diffraction (XRD) analysis is conducted using a Malvern PANalytical Empyrean Multicore High-Performance X-ray Diffractometer with an average wavelength of $Cu K_{\alpha 1}$ and $Cu K_{\alpha 2}$ radiation ($\lambda=0.15418$ nm, voltage: 45 kV, current: 40 mA) in the 2θ range from 10° to 50° , with a scanning step size of 0.02° , to investigate the crystallinity and phase characteristics of the PQD@GNC: Sm_2O_3 samples. Transmission electron microscopy (TEM) analysis is further used to verify the presence and size of PQDs in the GNC samples. Leveraging the brittleness of the samples, PQD@GNC: Sm_2O_3 specimens are ground into fine particles using an agate mortar to produce electron-transparent particles. These particles are then deposited onto a holey carbon copper grid. TEM analysis is performed on a JEOL JEM-2100 operating at 200 kV. Optical absorption spectra are recorded over the 300-1100 nm range using an Edinburgh Instruments DS5 UV-Vis spectrophotometer. The optical band gap values (E_g) of the PQD@GNC: Sm_2O_3 samples are calculated using the derivation of absorption spectrum fitting (DASF) method, which enables accurate calculation of band gap (E_g) values solely from absorption spectrum measurements, irrespective of thickness. Moreover, the DASF method allows for the identification of both E_g and

transition type without any prior assumptions regarding the nature of electronic transitions [48]. Photoluminescence (PL) spectra of the PQD@GNC:Sm₂O₃ samples in the 400-750 nm range, are obtained using an Edinburgh Instruments FS5 fluorescence spectrofluorometer equipped with a 150 W xenon lamp (signal-to-noise ratio of water Raman signal > 6000:1). The corresponding Commission Internationale d'Éclairage (CIE) 1931 color coordinates are derived from the PL emission spectra using OSRAM ColorCalculator software. The PLQY values are determined (with an estimated error of ±5%) using an integrating sphere (150 mm diameter internal spherical space, polytetrafluoroethylene-coated) under 464 nm excitation. The time-resolved lifetime spectra of PQD@GNC:Sm₂O₃ samples are measured using time-correlated single-photon counting technique with a picosecond pulse laser (450 nm) as the excitation source. The decay curves are fitted using a bi-exponential equation to achieve a χ^2 value close to unity:

$$I(t) = A_1 e^{\left(\frac{-t}{\tau_1}\right)} + A_2 e^{\left(\frac{-t}{\tau_2}\right)} \quad (1)$$

where, $I(t)$ is the emission intensity, τ_1 and τ_2 are the lifetime values, and A_1 and A_2 are the decay constants. The average lifetime for each transition is calculated using:

$$\tau_{meas} = \frac{A_1 \tau_1^2 + A_2 \tau_2^2}{A_1 \tau_1 + A_2 \tau_2} \quad (2)$$

Chemical durability tests are conducted by immersing the synthesized samples in deionized water at room temperature for 90 days. During this period, PL measurements are taken at regular intervals to assess the impact of humidity on the chemical durability of the samples. Temperature-dependent PL measurements, up to 150 °C, are performed using a Pike Technologies heated solid transmission attachment installed in the fluorescence spectrophotometer. In addition, photostability tests are carried out on selected samples under continuous 450 nm excitation. The samples remain in a fixed position within the spectrofluorometer while uninterrupted excitation is applied, and PL measurements are recorded hourly for the first 10 hours, followed by measurements every 10 hours

thereafter. An Asensetek Lighting Passport Pro Spectrometer and an IR thermometer are used to measure the light intensity and temperature of the constructed prototype plant growth LED.

3. Results and Discussion

3.1. Thermal and structural characterizations

The thermal characteristics of the samples are examined to accurately determine the appropriate annealing and heat-treatment conditions. Figure 1a shows the STA curve of the selected 0%Sm₂O₃-as-cast sample. The annealing temperature is set at 400 °C, below the glass transition temperature (T_g) of 502 °C, to prevent any potential crystallization of the glass matrix. In contrast, heat-treatment temperatures are chosen to be significantly higher than T_g to ensure the successful precipitation of PQDs within the glass host. Consequently, the as-cast samples are heat-treated at temperatures ranging from 590 °C to 620 °C, with 10 °C increments. Additionally, the STA results show that the synthesized samples can endure high temperatures while preserving their structural integrity, which is essential for LED applications.

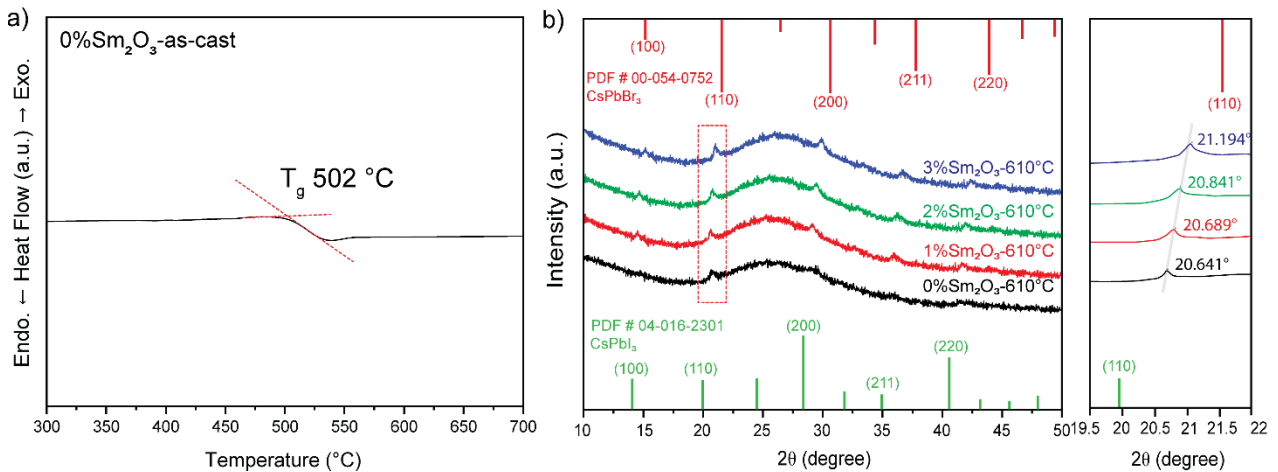


Figure 1. a) STA thermogram of the undoped as-cast sample (0%Sm₂O₃-as-cast), and b) XRD patterns of PQD@GNC:Sm₂O₃ samples with incremental Sm₂O₃ doping concentrations, all heat-treated at 610°C.

To confirm the crystallization of PQDs, Figure 1b shows the XRD patterns of PQD@GNC:Sm₂O₃ samples with incremental Sm₂O₃ doping concentrations, heat-treated at 610 °C. In addition to the broad halo observed in all samples, indicating their glassy nature, five distinct diffraction peaks are identified aligning with the standard card files for pure CsPbBr₃ (PDF #00-054-0752) and CsPbI₃ (PDF #04-016-2301) PQDs. This suggests that the cubic CsPbBr₁I₂ PQDs are successfully precipitated without any secondary phases or contaminants detected. With the incorporation of Sm₂O₃, the diffraction peaks become slightly sharper and more prominent compared to the 0%Sm₂O₃ sample, indicating an enhanced crystallization due to Sm₂O₃ doping. The right panel of Figure 1b shows a magnified view of the diffraction peaks for the (110) lattice planes of the PQDs. The 0%Sm₂O₃-610°C sample exhibits a diffraction peak at a 2θ value of 20.641°. With increasing Sm₂O₃ doping concentration, the 1%Sm₂O₃-610°C, 2%Sm₂O₃-610°C, and 3%Sm₂O₃-610°C samples show diffraction peaks at 2θ values of 20.689°, 20.841°, and 21.194°, respectively, indicating a gradual shift towards higher angles. This shift is attributed to the smaller ionic radius of Sm³⁺ (r = 0.96 Å) compared to Pb²⁺ (r = 1.19 Å), leading to lattice shrinkage and demonstrating successful integration of Sm³⁺ ions into the PQD crystals [49,50].

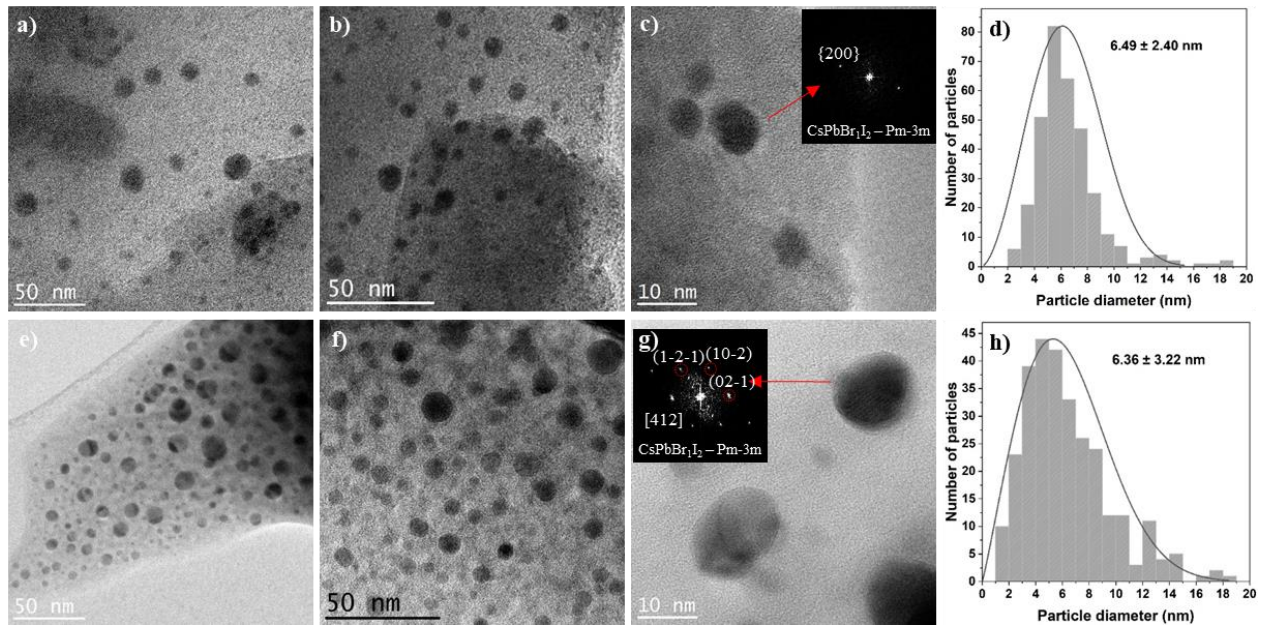


Figure 2. TEM analyses of PQD@GNC:Sm₂O₃ samples doped with 0%Sm₂O₃ (a-d, upper row) and 2%Sm₂O₃ (f-h, lower row). a) and b) Bright-field TEM images of the 0%Sm₂O₃-610°C sample, c) HRTEM image showing several PQDs within the glass matrix (inset shows the corresponding power spectra (FFT) of the indicated PQD), d) Particle size distribution histogram obtained by measuring more than 300 PQDs across different images, e) and f) Bright-field TEM images of the 2%Sm₂O₃-610°C sample, g) HRTEM image showing several PQDs within the glass matrix (inset shows the corresponding power spectra (FFT) of the indicated PQD), h) Particle size distribution histogram obtained by measuring more than 300 PQDs across different images.

The presence and particle size of PQDs within the glass matrix are further confirmed through TEM analysis (see Figure 2) for the selected undoped and 2%Sm₂O₃ doped PQD@GNC:Sm₂O₃ samples. It should be stressed here that the fact that the glass-matrix is sensitive to the e-beam makes obtaining HRTEM images rather challenging as the stable, crystalline PQDs move with the shrinking glass matrix even at electron flux values smaller than 124.8 e⁻/Å². Figure 2a and 2b display general bright-field TEM images of the 0%Sm₂O₃-610°C sample, highlighting the

distribution of PQDs with varying sizes within the glass matrix. Figure 2d presents a particle size distribution histogram, measured from over 300 PQDs across different images, showing an average PQD size of 6.49 ± 2.40 nm. It should be noted here that various PQD clusters with sizes larger than 80 nm, composed of the agglomeration of individual PQDs, are also observed for the sample (see Figure S1). These large clusters are not measured while obtaining the particle size distribution histogram. Figure 2c provides a HRTEM image, showing several PQDs embedded in the glass matrix. The inset of Figure 2c is the corresponding FFT of the indicated PQD (~ 9 nm), with observed spots with plane spacing of 0.2917 nm that fit well with the $\{200\}$ plane spacing (0.2935 nm) of the cubic perovskite phase (space group = Pm-3m). Figure 2e and 2f display general bright-field TEM images of the 2%Sm₂O₃-610°C sample, highlighting the distribution of PQDs with varying sizes within the glass matrix. As can be seen here and in the additional TEM images presented in Figure S2, unlike the 0%Sm₂O₃-610°C sample, no agglomerates of PQDs are observed for the 2%Sm₂O₃-610°C sample, indicating that Sm₂O₃ influences the crystallization behavior of PQDs. Figure 2h presents a particle size distribution histogram, measured from over 300 PQDs across different images, showing an average PQD size of 6.36 ± 3.22 nm. Figure 2f provides a HRTEM image, showing several PQDs embedded in the glass matrix. The inset of Figure 2e shows the FFT from the upper-right spherical PQD (~ 13 nm), revealing that this PQD is also composed of the same cubic perovskite phase, and oriented along the [421] zone axes.

3.2. Optical absorption characteristics

Figures 3a and 3b show digital images of PQD@BSC:Sm₂O₃ samples under daylight and UV light, respectively. Following the heat-treatment process, all samples exhibit a reddish color change, indicating the crystallization of PQDs within the glass matrix. No significant color change is observed among samples with the same Sm₂O₃ concentration as the temperature varies. However, as the Sm₂O₃ doping concentration increases, the samples transition in color from dark red to bright

red. Samples with 0% and 1% Sm₂O₃ doping display nonuniform crystallization across all heat-treatment temperatures, whereas those with 2% and 3% Sm₂O₃ doping demonstrate a more uniform crystallization of PQDs. This suggests that higher Sm₂O₃ doping concentrations influence the CsPbBr₁I₂ PQD structure through the incorporation of Sm³⁺ ions, thereby promoting uniform crystallization. This finding aligns with the TEM results (Figures 2 and S1), where some large agglomerates are observed for the undoped sample, and the XRD results (see Figure 1b), where the diffraction peaks of Sm₂O₃-doped samples become more pronounced compared to the undoped sample and the peak intensity increases with higher Sm₂O₃ doping concentrations.

Figure 3c shows the optical absorption spectra of PQD@BSC:Sm₂O₃ samples heat-treated at various temperatures. The first excitonic peak, corresponding to the CsPbBr₁I₂ PQDs is marked with a red asterisk, further confirming the successful formation of PQDs. To better illustrate the spectral shift caused by increasing Sm₂O₃ concentration, the right panel of Figure 3c presents the absorbance peaks of samples heat-treated at 610 °C. As the Sm₂O₃ concentration increases, the size of PQDs tends to decrease, which results in a blue shift in the absorption spectra. This can be attributed to the enhanced nucleation of PQDs at higher Sm₂O₃ concentrations, which favors the formation of smaller PQDs but hinders their further growth due to depletion of available perovskite components in the glass matrix [51]. Additionally, as the heat treatment temperature increases, the absorption edge shifts to longer wavelengths (a red shift), indicating more uniform crystallization and a modification of the PQD structure. The undoped (0% Sm₂O₃-doped) PQD@GNC samples show no visible absorption peaks. In contrast, the 1% and 2% Sm₂O₃-doped PQD@GNC samples display four absorption peaks at 402, 474, 942, and 1073 nm, corresponding to the transitions ⁶H_{5/2} → ⁶P_{3/2}, ⁶H_{5/2} → ⁴I_{11/2}, ⁶H_{5/2} → ⁶F_{11/2}, and ⁶H_{5/2} → ⁶F_{9/2}, respectively, which are characteristic of the Sm³⁺ ion [52]. However, the absorption peaks at 402 and 474 nm associated with the Sm³⁺ ion

become increasingly difficult to observe in the 3% Sm₂O₃-doped PQD@GNC samples, likely due to the increasing absorbance.

Figure 3d shows the variation of $[\ln(A\lambda^{-1})/d\lambda^{-1}]$ versus (λ^{-1}) (DASF plots) for the PQD@GNC:Sm₂O₃ samples doped with 0%Sm₂O₃, 1%Sm₂O₃, 2%Sm₂O₃, and 3%Sm₂O₃, all heat treated at 610 °C. All DASF plots exhibit a discontinuity at $\lambda^{-1} = \lambda_g^{-1}$; thus, the E_g values are calculated by determining the λ_g values, as E_g can be derived using the formula $1239.83/\lambda_g$. The E_g of 0%Sm₂O₃-610°C sample is calculated as 1.91 eV, while the E_g values for the 1%Sm₂O₃-610°C, 2%Sm₂O₃-610°C, and 3%Sm₂O₃-610°C samples are calculated as 1.96, 1.99, and 2.01 eV, respectively, showing a systematic increase with increasing Sm₂O₃ concentration. The increase in band gap energy is attributed to two factors. First, the integration of Sm³⁺ ions into the PQD lattice causes lattice shrinkage, which increases the energy difference between the conduction band and the valence band, resulting in a larger band gap. Second, Sm³⁺ ions enhance the crystallization of the QDs, but since the perovskite components in the glass matrix are limited, the PQDs crystallize more easily but their growth is restricted, leading to smaller PQDs. This reduction in PQD size further strengthens the electron confinement effect, which also contributes to the observed increase in band gap. Additionally, this behavior suggests a decrease in the number of shallow defect energy levels, which may further influence the optical properties of the PQDs [37].

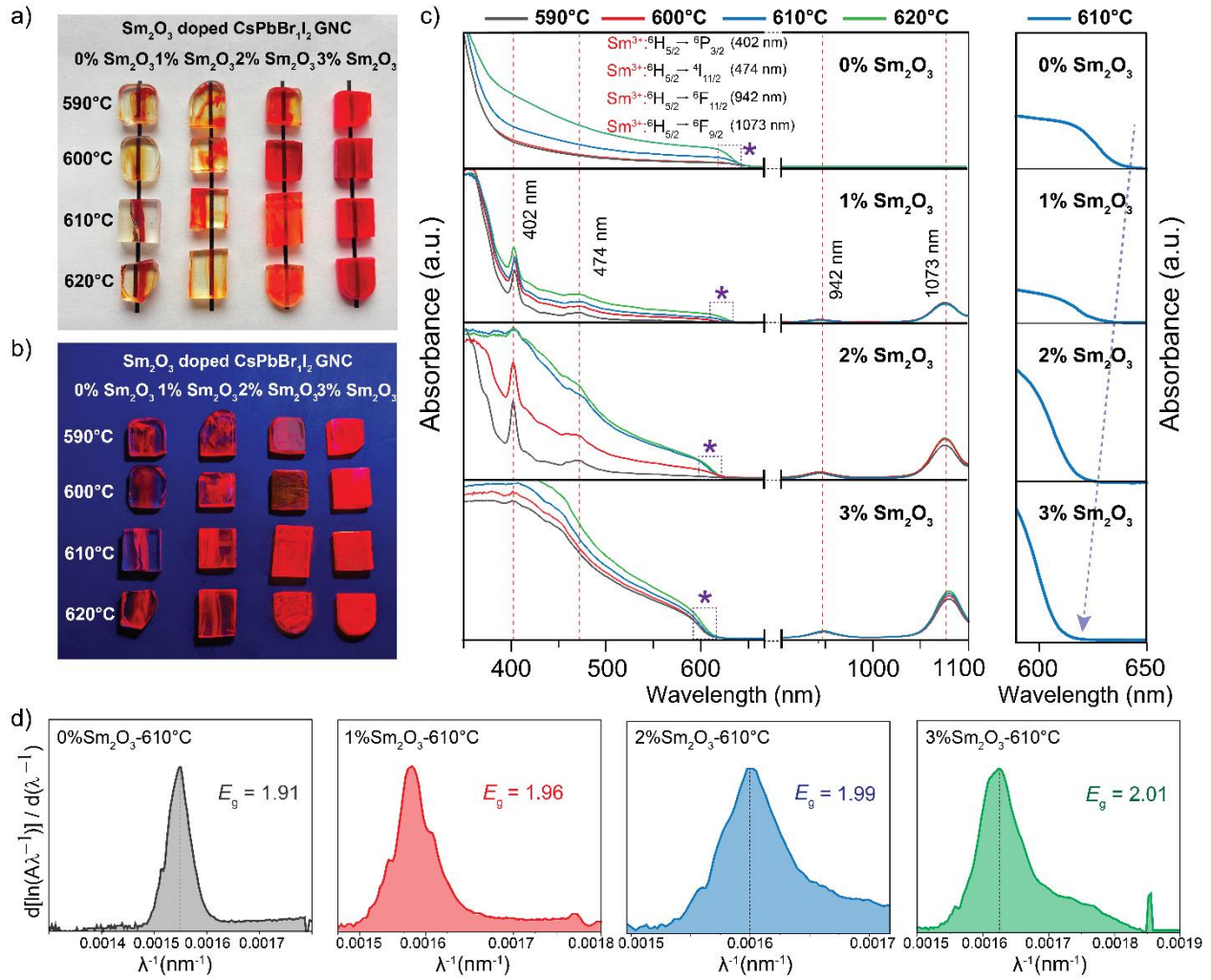


Figure 3. Photographs under a) daylight and b) UV light illumination, c) absorbance spectra for four different PQD@GNC:Sm₂O₃ sample sets, and d) DASF plots of $d[\ln(A\lambda^{-1})]/d\lambda^{-1}$ versus (λ^{-1}) for PQD@GNC:Sm₂O₃ samples doped with 0%Sm₂O₃, 1%Sm₂O₃, 2%Sm₂O₃, and 3%Sm₂O₃, all heat-treated at 610 °C.

3.3. Photoluminescence properties and energy transfer mechanisms

The PL emission spectra of PQD@GNC:Sm₂O₃ samples, recorded under continuous 464 nm excitation, are shown in Figure 4a-d. All PL emissions are normalized to facilitate a better comparison between different Sm₂O₃-doping concentrations and heat-treatment temperatures. As clearly observed, the PL peak positions of the 0%Sm₂O₃ samples exhibit a slight redshift from 629

nm to 635 nm as the heat-treatment temperature increases from 590°C to 620°C, corresponding to the emission of CsPbBr₁I₂ PQDs. For the samples doped with 1%Sm₂O₃, 2%Sm₂O₃, and 3%Sm₂O₃, the same PL emission peak positions show a more pronounced redshift from 622 nm to 634 nm, 618 nm to 633 nm, and 617 nm to 631 nm, respectively, with the same increase in heat-treatment temperature. These findings align with the principle that an increase in PQD size due to higher heat-treatment temperatures leads to light emission at longer wavelengths upon photon excitation, compared to samples heat-treated at lower temperatures. Although, the shape of the PL bands is not significantly affected by the dopant concentration or heat-treatment temperature, the incorporation of Sm³⁺ ions to PQD structure makes four main PL peaks of Sm³⁺ visible, corresponding to the transitions from ⁴G_{5/2} to ⁶H_{5/2}, ⁶H_{7/2}, ⁶H_{9/2}, and ⁶H_{11/2}, respectively for the samples doped with 1%Sm₂O₃, 2%Sm₂O₃. However, in the sample doped with 3%Sm₂O₃, the red emission from the PQDs suppresses the Sm³⁺ emissions, rendering the PL peaks of Sm³⁺ invisible. Figure 4e presents the PL emission spectra for samples with varying Sm₂O₃ doping concentrations, all heat-treated at a selected temperature of 610°C. The PL emission intensity is observed to initially increase with Sm₂O₃ doping, reaching a maximum at the 2%Sm₂O₃-610 °C sample, before decreasing for the 3%Sm₂O₃-610 °C sample. This decline in intensity is attributed to an increased number of non-radiative recombination events caused by the high Sm³⁺ concentration, a phenomenon known as concentration quenching. At higher Sm³⁺ concentrations, the ions become closer together in the glass matrix, leading to an increased probability of non-radiative processes such as cross-relaxation and resonance energy transfer between Sm³⁺ ions. These processes can effectively dissipate the excitation energy without emitting photons, thereby reducing the overall PL intensity. The concentration quenching effect becomes more prominent when the interactions between the ions are stronger, which occurs as the average distance between the Sm³⁺ ions decreases in the matrix [53]. Moreover, as the Sm₂O₃ doping increases, a blue shift in the PL peak

positions for all heat-treated samples is observed, which is consistent with the widening of the band gap due to lattice contraction. The inset graph shows the PL excitation spectra recorded for the 629 nm PL emission, indicating that the selected 464 nm excitation wavelength is an efficient excitation source. The CIE color coordinates further confirm that all observed emissions fall within the red region.

Figure 4f shows the PLQY values for samples with varying Sm_2O_3 doping concentrations, heat-treated at varying temperatures between 590 and 620 °C. An initial increase in PLQY is observed across all samples as the heat-treatment temperature rises to 610 °C, followed by a decline at 620 °C. For example, the samples doped with 2% Sm_2O_3 exhibit PLQY values of 12.0%, 33.2%, 44.3%, and 25.7% at 590 °C, 600 °C, 610 °C, and 620 °C, respectively. Notably, the 2% Sm_2O_3 -610°C sample achieves an impressive PLQY of 44.3%, the highest among all synthesized samples, and is considered notably high in comparison with values reported in similar works in the literature with bromide-iodide PQDs [54]. Therefore, the 2% Sm_2O_3 -610°C sample is selected for further studies in plant growth LED construction due to its superior PLQY performance.

Time-resolved PL spectra of the $\text{PQD@GNC:Sm}_2\text{O}_3$ samples, all heat-treated at 610 °C, are given in Figure 4g. The spectra are recorded by monitoring the most intense emissions for each sample under a constant 450 nm excitation. All lifetime parameters, including non-radiative (τ_1), radiative (τ_2), and average (τ_{average}), are provided in Table S1. The decreasing trend in τ_2 and τ_{average} support the occurrence of non-radiative energy transfer to Sm^{3+} ions in the Sm_2O_3 doped samples [37,39,55]. In addition, the short lifetime (τ_1), associated with non-radiative recombinations caused by trap states, for the $\text{PQD@GNC:Sm}_2\text{O}_3$ samples doped with 0% Sm_2O_3 , 1% Sm_2O_3 , 2% Sm_2O_3 , and 3% Sm_2O_3 are observed as 21 ns, 23 ns, 15 ns, and 8 ns, respectively. The overall decrease in short lifetime values can be attributed to the reduction in defect levels within the bandgap of the CsPbBr_3 PQD structure, facilitated by the incorporation of Sm^{3+} ions [37,46,56]. Although direct

measurement of the Sm^{3+} ion emission lifetime is not possible, a slight decrease is expected due to Sm^{3+} clustering during heat treatment, which may create nucleation sites for PQDs and enhance the energy transfer process. [39].

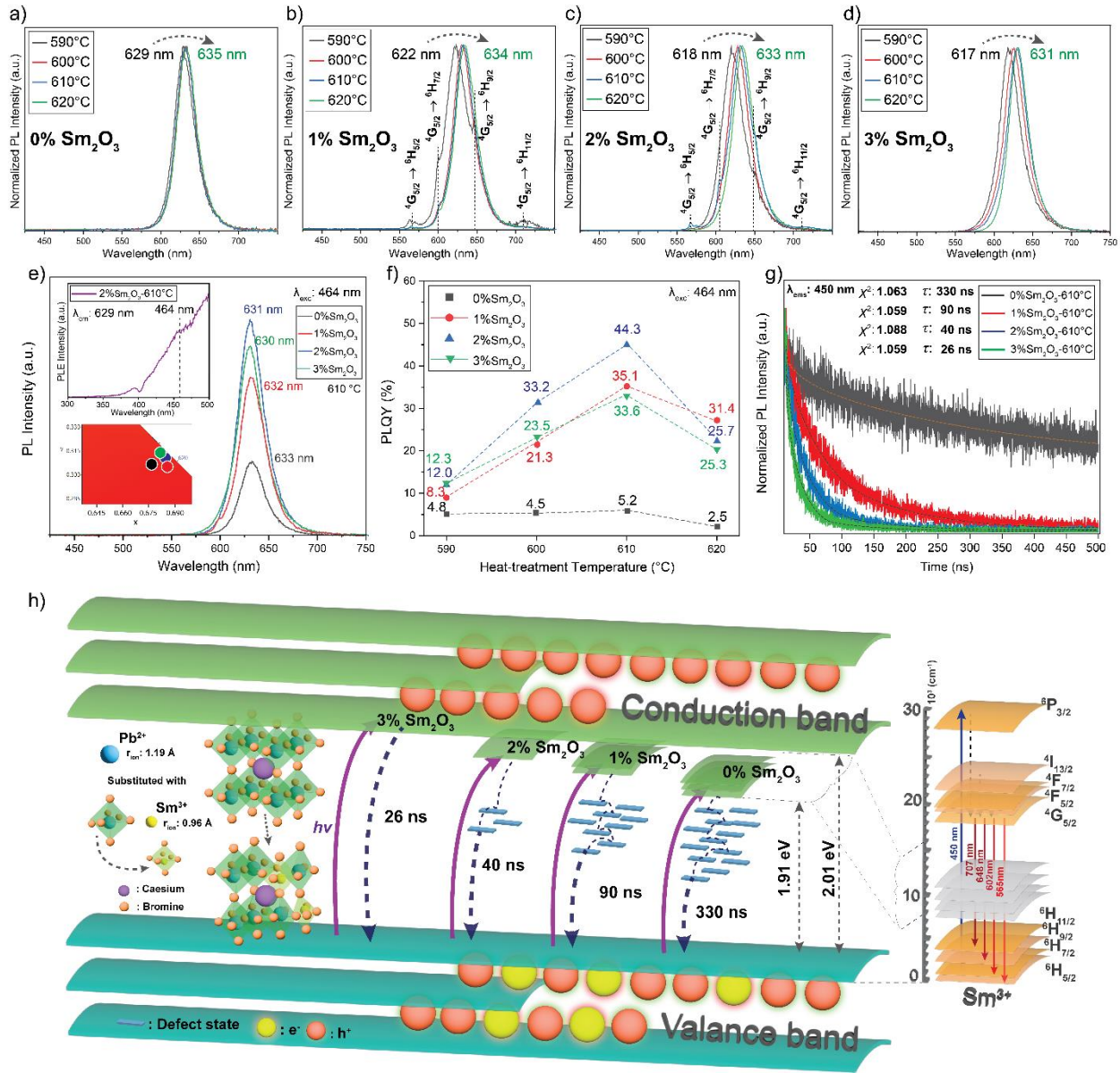


Figure 4. a-d) PL emission spectra of PQD@GNC: Sm_2O_3 samples doped with 0% Sm_2O_3 , 1% Sm_2O_3 , 2% Sm_2O_3 , and 3% Sm_2O_3 , heat-treated at varying temperatures between 590 and 620 °C, e) PL emission spectra of PQD@GNC: Sm_2O_3 samples doped with 0% Sm_2O_3 , 1% Sm_2O_3 , 2% Sm_2O_3 , and 3% Sm_2O_3 , all heat-treated at 610 °C, f) PLQY values of PQD@GNC: Sm_2O_3

samples doped with 0%Sm₂O₃, 1%Sm₂O₃, 2%Sm₂O₃, and 3%Sm₂O₃, heat-treated at varying temperatures between 590 and 620 °C, g) time-resolved PL spectra of PQD@GNC:Sm₂O₃ samples doped with 0%Sm₂O₃, 1%Sm₂O₃, 2%Sm₂O₃, and 3%Sm₂O₃, all heat-treated at 610 °C, recorded at a fixed monitoring wavelength of 632 nm—corresponding to the average of the most intense emissions across all samples—under 450 nm pulsed laser excitation. (all PL emissions and PLQY measurements are recorded under 464 nm continuous excitation wavelength.), and h) effect of Sm₂O₃ doping on the CsPbBr₁I₂ PQD structure, showing changes in lattice properties and energy transfer mechanisms.

Figure 4h illustrates the effect of Sm₂O₃ doping on the CsPbBr₁I₂ PQD structure, highlighting changes in lattice properties and energy transfer mechanisms. The CsPbBr₁I₂ PQD structure remains largely unchanged with increasing Sm₂O₃ concentration, indicating that Sm₂O₃ doping does not alter the cubic crystal form of CsPbBr₁I₂ PQDs. However, lattice shrinkage is observed, as evidenced by the XRD analysis in Figure 1b, and this structural distortion is illustrated on the left side of Figure 4e. The potential resulting phenomena from Sm₂O₃ doping to the CsPbBr₁I₂ PQD structure can be summarized as follows: (1) increasing bandgap due to lattice shrinkage with higher Sm³⁺ content; (2) more uniform crystallization of CsPbBr₁I₂ PQDs as Sm³⁺ ions acting as nucleating agents; (3) reduction in lattice defects with increasing Sm³⁺ content, supported by short lifetime measurements; and (4) increasing overlap between the Sm³⁺ energy band and the PQD conduction band as Sm³⁺ content increases [37,51,56-58]. Additionally, the right side of Figure 4h presents a partial Jablonski diagram, with accurately positioned eV values to demonstrate the behavior of Sm³⁺ ions under UV excitation. When excited with a 450 nm LED chip, Sm³⁺ ions transition from their ground state ⁶H_{5/2} to the excited state ⁶P_{3/2}. They then undergo various non-radiative energy transfers to the ⁴G_{5/2} energy state followed by relaxation to the ⁶H_n (n = 5/2, 7/2, 9/2, and 11/2) states, resulting in emissions at 565 nm, 602 nm, 648 nm, and 707 nm.[46] Such an

energy transfer is plausible due to the correlation of energy levels; however, the energy levels of PQDs exhibit much broader absorption coefficients. Since the PL peaks of Sm^{3+} ions could not be separately detected, it can be inferred—based solely on lifetime analysis—that energy transfer from the perovskite structure to Sm^{3+} ions may be occurring [59].

3.4. Chemical, thermal and photo stability properties

Temperature-dependent PL spectra of the 2% Sm_2O_3 -610°C sample are recorded at temperatures ranging from 25 °C to 150 °C to assess the thermal stability of PQDs within the glass structure (see Figure 5a). The characteristic red emission of PQD@GNC: Sm_2O_3 gradually diminishes as the temperature increases from 25 °C to 150 °C, due to the multi-phonon-assisted non-radiative electron relaxation (thermal quenching) mechanism. However, the PL emission intensity measured at 100 °C retains more than 67% of the initial intensity recorded at 25 °C. Additionally, the broad emission band of the 2% Sm_2O_3 -610°C sample maintains its original position despite the temperature change, indicating no shift in band position.

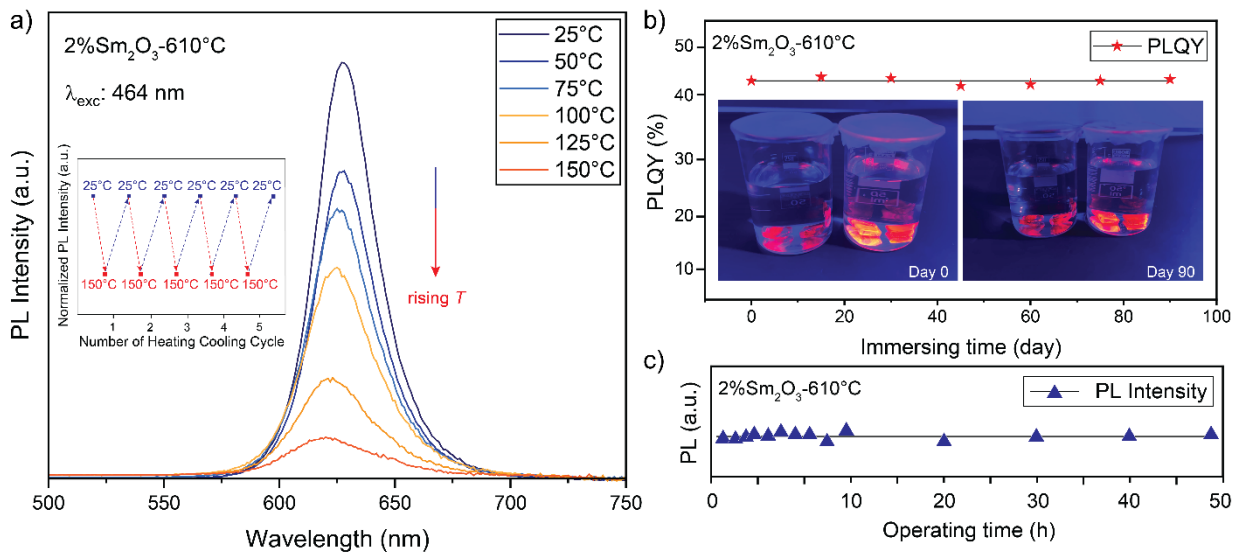


Figure 5. a) Temperature-dependent PL emission spectra (inset shows the heating-cooling cycles from 25 °C to 150 °C), b) PLQY values recorded at different time intervals after immersion in

water for up to 90 days, and c) photostability measurements for the selected 2%Sm₂O₃-610°C sample (Thermal and chemical stability measurements are conducted under 464 nm excitation, while photostability measurements are performed under continuous 450 nm excitation.). Heating-cooling cycle experiments, involving up to 5 consecutive cycles from 25 °C to 150 °C, are performed to evaluate the impact of temperature on the PL intensity of PQD@GNC:Sm₂O₃. As shown in the inset of Figure 5a, the reduction in PL emission intensity at higher temperatures nearly reverts to its original value even after five successive heating-cooling cycles. Furthermore, the selected 2%Sm₂O₃-610°C sample is immersed in water for up to 90 days to test the chemical durability of glass-encapsulated PQDs against moisture. As shown in Figure 5b, no significant decrease in PLQY values is observed even after 90 days, indicating the effectiveness of the selected glass host's encapsulation. Additionally, the photograph in Figure 5b displays two samples produced under identical conditions at different times to assess the repeatability of the synthesis process, confirming that no observable differences occurred between them. Figure 5c presents the photostability graph of the selected 2% Sm₂O₃-610°C sample under continuous 450 nm excitation. As evident from the intensity values, even under prolonged excitation, the 2% Sm₂O₃-610°C sample retains its luminescence properties exceptionally well, confirming its suitability for applications requiring long-term stability. This result can be attributed to the robust structure of the borosilicate glass matrix, which prevents any degradation from potential interactions between the PQDs and moisture.

3.5. Plant growth LED studies

To evaluate the photoelectric conversion efficiency of the 2% Sm₂O₃-610°C sample, the internal quantum efficiency (IQE, η_{int}), external quantum efficiency (EQE, η_{ext}), and absorption efficiency (AE, ϵ_{abs}) are calculated as described in previous studies [60,61]. The emission spectra measured

inside the integrating sphere with and without the sample, are shown in Figure S3. The calculated values for IQE, AE, and EQE are 51.28%, 49.62%, and 25.44%, respectively.

Subsequently, a plant growth LED, named PQD:Sm-LED, is fabricated by attaching the selected PQD@GNC:2%Sm₂O₃-610°C sample to blue LED chip emitting at 450 nm. The photosynthetic photon flux density (PPFD) of PQD:Sm-LED is adjusted to 27 $\mu\text{mol}\cdot\text{m}^{-2}\cdot\text{s}^{-1}$, featuring a CIE color coordinate of (x=0.3756, y=0.2575) and a luminous efficiency of radiation (LER) of 171 lm/W. Figure 6a presents the electroluminescence and photoluminescence spectra of the PQD:Sm-LED, highlighting their intersections with the absorption curves of chlorophyll a, chlorophyll b, carotenoids, and far-red phototropins. A digital image of the PQD:Sm-LED in operation is shown as an inset. Figure 6a clearly shows that the constructed PQD:Sm-LED efficiently stimulates the pigments essential for plant growth.

A commercial WLED with a PPFD of 80 $\mu\text{mol}\cdot\text{m}^{-2}\cdot\text{s}^{-1}$ is also used for experimental purposes. Two LED panels are then manufactured by combining the PQD:Sm-LED and WLED, resulting in an experimental LED panel and a control LED panel consisting solely of WLEDs. The total PPFD of both LED panels is kept almost constant at around 240 $\mu\text{mol}\cdot\text{m}^{-2}\cdot\text{s}^{-1}$, with a 16-hour photoperiod providing a daily light integral of 13.5 $\text{mol}\cdot\text{m}^{-2}\cdot\text{day}^{-1}$ for each panel. Notably, since plants have photoreceptors active across the entire visible spectrum that influence their growth, a WLED is added to the experimental panel for better comparison.[49] Therefore, 6×PQD:Sm-LED and a WLED are mounted onto the experimental LED panel, while 3×WLEDs are used for the control LED panel, both attached to aluminum plates for cooling. The arrangement of the LED panels within a controlled plant growth chamber is illustrated in the digital image provided in Figure 6b. Two basil samples, grown from seeds harvested from the same plant, are sown and placed into the chamber, which is divided into two sections. All other experimental details for the plant tests follow the procedures outlined in our previous study [19]. It is observed that the plant grown under the

experimental LED panel exhibits a longer stem and larger leaves compared to the plant grown under the control LED panel. Notably, as this experiment serves as a preliminary study aimed at demonstrating the performance of the manufactured PQD:Sm-LED, the data obtained should be reassessed through more detailed plant growth experiments.

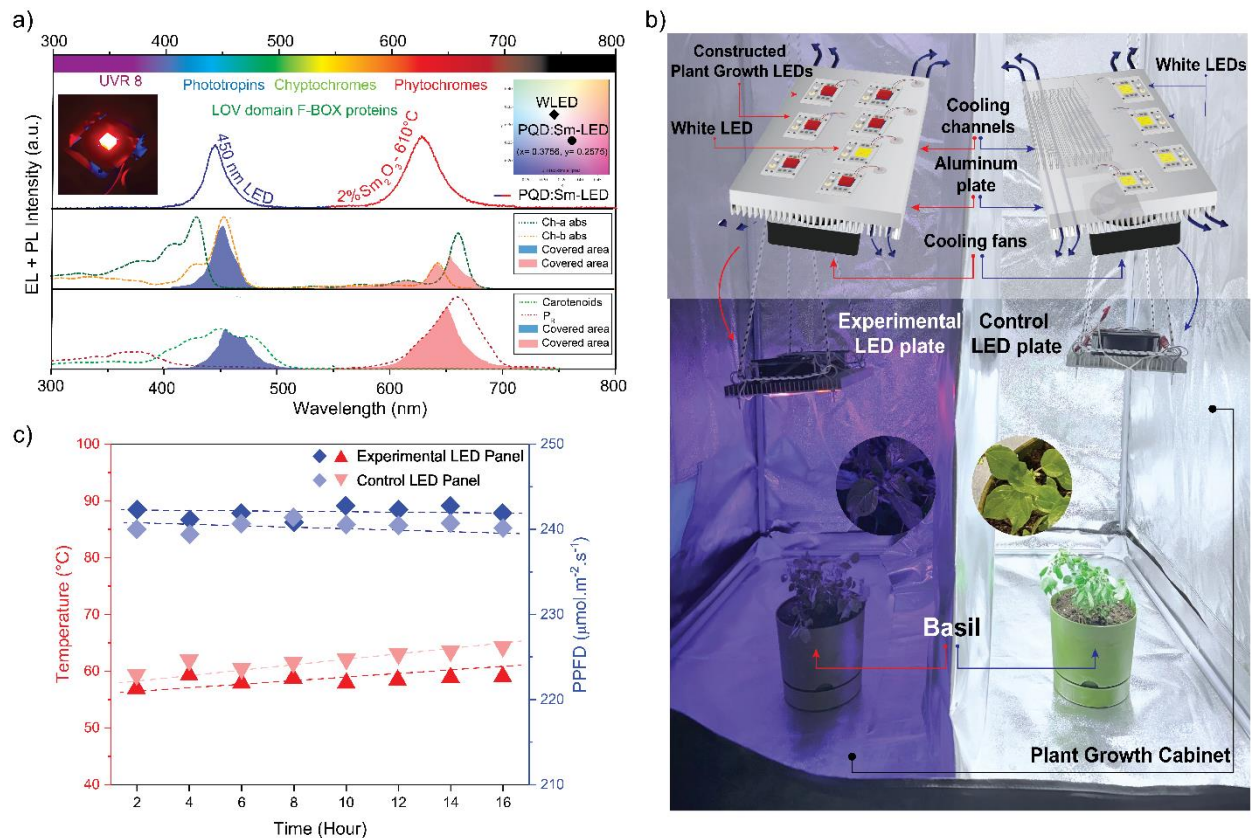


Figure 6. a) Electroluminescence and photoluminescence spectra of the PQD:Sm-LED, showing intersections with the absorption curves of chlorophyll a and b, carotenoids, and far-red phototropins, b) illustrative representation of the LED panels and a digital image of the plant growth cabinet equipped with the experimental LED panel (left) and the control LED panel (right), and c) variations in PPFD and temperature of the experimental and control LED panels over a 16-hour photoperiod.

Figure 6c shows the average operating temperatures and PPFD regimes for both LED panels. The results clearly demonstrate that the cooling system effectively maintains the LED panels within

acceptable temperature limits. Additionally, the PPFD levels for both panels show a slight decrease during operation due to the slightly increasing operating temperatures of the LED panels but recover at the beginning of the next photoperiod. The lack of any significant shift in the LED panels' operating temperature and light intensity over time indicates that they do not experience issues such as fatigue or performance degradation during the photoperiodic cycle.

Table 1. Colorimetric properties of selected PQD@GNC:Sm₂O₃ used in the LED prototype, compared with data reported for various luminophores incorporated into PiGs, GNCs, glasses, and glass ceramics for plant growth LED applications.

Year	Luminophore	QY (%)	PL peak position (nm)	Excitation Source (nm)	Plant Type	CIE (x,y)	Light Intensity ($\mu\text{mol.m}^{-2}.\text{s}^{-1}$)	LER (lm/W)	Ref.
2018	ZnGa ₂ O ₄ :Cr ³⁺ PiG	52.8	710	400	-	0.6620- 0.2560	-	-	[42]
2018	MgO.MgF ₂ .GeO ₂ :Mn ⁴⁺ PiG	27.5	659	420	Milk- Chinese cabbage	0.4189- 0.1388	110	-	[62]
2019	CsPbCl ₂ Br ₁ GNC	24.0	523	460	Pak choi Cabbage	-	-	-	[63]
2019	CsPb0.7Ti _{0.3} I ₃ GNC	30.8	683	450	-	0.3412- 0.3621	-	102.44	[64]
2020	CsPbCl/I ₃ GNC	44.9	677	400	Napa cabbage	-	-	-	[65]
2020	Ba _{1.3} Sr _{1.7} MgSi ₂ O ₈ :Eu ²⁺ , Mn ²⁺ PiG	45.3	655	370	Romaine lettuce	-	-	-	[66]
2021	CsPbCl ₃ :Mn ⁴⁺ GNC	-	625	450	Cabbage	-	-	-	[45]
2021	CsPbBrI ₂ :Gd ³⁺ GNC	37	630	460	-	0.3340- 0.3386	-	90.09	[43]
2023	Sm ³⁺ /Tm ³⁺ doped Glass	56	602	360	Romaine lettuce	-	150	-	[19]

2024	CsPbBr _{3-x} I _x GNC	52.7	650	460	-	0.6420- 0.2710	-	26.27	[67]
2024	CsSbBr ₃ /SnO ₂ Glass- ceramic	51.5	White	288	Pea plant	0.2847- 0.3281	-	-	[68]
2024	PQD@GNC:2%Sm ₂ O ₃ - 610°C	44.6	630	450	Basil	0.3756- 0.2575	240	171	Current Work

Table 1 presents the colorimetric properties of the constructed PQD:Sm-LED, alongside previously reported plant growth LEDs that use various luminophores in PiGs, GNCs, glasses, and glass ceramics. The data show that the constructed PQD:Sm-LED with a selected 2%Sm₂O₃-610°C sample performs either comparably to or better than earlier reports. While direct comparisons of real-time plant growth results are challenging due to differing test conditions in previous studies, the positive outcomes observed underscore the potential of PQD:Sm-LED for enhancing indoor plant cultivation. These results are pivotal for advancing indoor horticulture and plant growth environments. Leveraging the positive outcomes of this study, upcoming research will expand to include diverse agricultural settings and a broader spectrum of plant species.

Conclusions

In summary, various sets of Sm₂O₃-doped CsPbBr₃I₂ PQD GNCs are synthesized using the melt-quenching technique, followed by controlled heat treatment to explore the effect of different Sm₂O₃ doping concentrations on the properties of these GNCs and optimize their emission for enhanced plant growth. XRD results show a slight shift to higher angles, indicating lattice shrinkage due to the substitution of Pb²⁺ ions with Sm³⁺ ions. This shrinkage increases the optical bandgap, enhancing quantum confinement, as evidenced by the blue shift in PL peaks at higher Sm₂O₃ concentrations. Additionally, the PL lifetime decreases with increasing Sm₂O₃ doping, likely due to a reduction in defect levels. The 2%Sm₂O₃-610°C sample exhibits an exceptional PLQY of

44.3%, the highest reported for CsPbBr_xI_(3-x) PQD GNCs. These high-performance samples are integrated with 450 nm blue LED chips to develop a plant growth LED panel, achieving a PPFD of 240 $\mu\text{mol}\cdot\text{m}^{-2}\cdot\text{s}^{-1}$, a luminous efficacy of 171 lm/W, and CIE color coordinates of $x = 0.3756$ and $y = 0.2575$. Plant growth tests show that plants exposed to the developed plant growth LED system exhibit longer stems and larger leaves compared to those grown under a standard commercial white LED system. Furthermore, the plant growth LED demonstrates excellent durability, withstanding temperature fluctuations and prolonged operation, while effectively stimulating key pigments essential for plant growth. The findings demonstrate that Sm₂O₃-doped CsPbBr₁I₂ PQD GNCs are promising candidates for next-generation plant growth lighting systems, providing an innovative and highly efficient solution for indoor farming that can significantly enhance plant cultivation techniques and contribute to further advancements in the field.

Acknowledgments

This work was supported by Yildiz Technical University Scientific Research Projects Coordination Unit under project number FBA-2023-5280. This research was also funded by the European Union under the Horizon Europe program (Project PV4Plants: AgriPV system with climate, water, and light spectrum control for safe, healthier, and improved crop production, Grant No. 101096409, Topic HORIZON-CL5-2022-D3-01-06). We acknowledge this support, which has been essential in advancing luminescent glass color converters and enabling spectrum engineering applied to plant growth lighting. We would like to also acknowledge the CCI Electron Microscopy Facility which has been part-funded by the European Regional Development Fund through the Welsh European Funding Office, and The Wolfson Foundation.

CRedit authorship contribution statement

Utku Ekim: Investigation, Visualization, Writing – original draft, Validation **Emre İltir:** Investigation, Visualization, Writing – original draft, Validation **Harun Samet Çelik:** Investigation

Aziz Genç: Investigation, Validation, Writing – review & editing **Thomas J. A. Slater:** Validation, Writing – review & editing **Miray Çelikbilek Ersundu:** Conceptualization, Writing – review & editing, Validation, Supervision, Project administration, Funding acquisition. **Ali Erçin Ersundu:** Conceptualization, Writing – original draft, Writing – review & editing, Validation, Supervision, Project administration, Funding acquisition.

Conflict of Interest

The authors declare no competing financial interest.

Data availability

The data supporting this article are available within the main article as well as its supporting information.

References

- [1] R. Wang, X. Yang, X. Chen, X. Zhang, Y. Chi, D. Zhang, S. Chu, P. Zhou, A critical review for hydrogen application in agriculture: Recent advances and perspectives, *Crit Rev Environ Sci Technol* 54 (2024) 222–238. <https://doi.org/10.1080/10643389.2023.2232253>.
- [2] S. Kumari, F. Nazir, C. Maheshwari, H. Kaur, R. Gupta, K.H.M. Siddique, M.I.R. Khan, Plant hormones and secondary metabolites under environmental stresses: Enlightening defense molecules, *Plant Physiology and Biochemistry* 206 (2024) 108238. <https://doi.org/10.1016/j.plaphy.2023.108238>.
- [3] P. Bhadra, S. Maitra, T. Shankar, A. Hossain, S. Praharaj, T. Aftab, Climate change impact on plants: Plant responses and adaptations, in: *Plant Perspectives to Global Climate Changes*, Elsevier, 2022: pp. 1–24. <https://doi.org/10.1016/B978-0-323-85665-2.00004-2>.
- [4] M. Zhang, Y. Ming, H.-B. Wang, H.-L. Jin, Strategies for adaptation to high light in plants, *ABIOTECH* 5 (2024) 381–393. <https://doi.org/10.1007/s42994-024-00164-6>.
- [5] A. Paliwal, A. Verma, H. Tiwari, M.K. Singh, J.K. Gour, A.K. Nigam, R. Kumar, V.B. Sinha, Effect and Importance of Compatible Solutes in Plant Growth Promotion Under Different Stress Conditions, in: *Compatible Solutes Engineering for Crop Plants Facing Climate Change*, Springer International Publishing, Cham, 2021: pp. 223–239. https://doi.org/10.1007/978-3-030-80674-3_10.
- [6] X. Mu, Y. Chen, The physiological response of photosynthesis to nitrogen deficiency, *Plant Physiology and Biochemistry* 158 (2021) 76–82. <https://doi.org/10.1016/j.plaphy.2020.11.019>.

- [7] E.A. Ainsworth, S.P. Long, What have we learned from 15 years of free-air CO₂ enrichment (FACE)? A meta-analytic review of the responses of photosynthesis, canopy properties and plant production to rising CO₂, *New Phytologist* 165 (2005) 351–372. <https://doi.org/10.1111/j.1469-8137.2004.01224.x>.
- [8] E. Huq, C. Lin, P.H. Quail, Light signaling in plants—a selective history, *Plant Physiol* 195 (2024) 213–231. <https://doi.org/10.1093/plphys/kiac110>.
- [9] N. Fukuda, Plant Growth and Physiological Responses to Light Conditions, in: *Plant Factory Using Artificial Light*, Elsevier, 2019: pp. 71–77. <https://doi.org/10.1016/B978-0-12-813973-8.00008-7>.
- [10] H. Dou, G. Niu, Plant responses to light, in: *Plant Factory*, Elsevier, 2020: pp. 153–166. <https://doi.org/10.1016/B978-0-12-816691-8.00009-1>.
- [11] M. de Wit, V.C. Galvão, C. Fankhauser, Light-Mediated Hormonal Regulation of Plant Growth and Development, *Annu Rev Plant Biol* 67 (2016) 513–537. <https://doi.org/10.1146/annurev-arplant-043015-112252>.
- [12] P.M. Pattison, J.Y. Tsao, G.C. Brainard, B. Bugbee, LEDs for photons, physiology and food, *Nature* 563 (2018) 493–500. <https://doi.org/10.1038/s41586-018-0706-x>.
- [13] A. Barceló-Muñoz, M. Barceló-Muñoz, A. Gago-Calderon, Effect of LED Lighting on Physical Environment and Microenvironment on In Vitro Plant Growth and Morphogenesis: The Need to Standardize Lighting Conditions and Their Description, *Plants* 11 (2021) 60. <https://doi.org/10.3390/plants11010060>.
- [14] G.B. Nair, H.C. Swart, S.J. Dhoble, A review on the advancements in phosphor-converted light emitting diodes (pc-LEDs): Phosphor synthesis, device fabrication and characterization, *Prog Mater Sci* 109 (2020) 100622. <https://doi.org/10.1016/j.pmatsci.2019.100622>.
- [15] Y.H. Kim, P. Arunkumar, B.Y. Kim, S. Unithrattil, E. Kim, S.-H. Moon, J.Y. Hyun, K.H. Kim, D. Lee, J.-S. Lee, W. Bin Im, A zero-thermal-quenching phosphor, *Nat Mater* 16 (2017) 543–550. <https://doi.org/10.1038/nmat4843>.
- [16] C. Yang, W. Liu, Q. You, X. Zhao, S. Liu, L. Xue, J. Sun, X. Jiang, Recent Advances in Light-Conversion Phosphors for Plant Growth and Strategies for the Modulation of Photoluminescence Properties, *Nanomaterials* 13 (2023) 1715. <https://doi.org/10.3390/nano13111715>.
- [17] Y. Xiao, W. Xiao, D. Wu, L. Guan, M. Luo, L. Sun, An Extra-Broadband VIS-NIR Emitting Phosphor toward Multifunctional LED Applications, *Adv Funct Mater* 32 (2022) 2109618. <https://doi.org/10.1002/adfm.202109618>.
- [18] Y. Zhou, C. Li, Y. Wang, Crystal-Field Engineering Control of an Ultraviolet–Visible-Responsive Near-Infrared-Emitting Phosphor and Its Applications in Plant Growth, Night Vision, and NIR Spectroscopy Detection, *Adv Opt Mater* 10 (2022) 2102246. <https://doi.org/10.1002/adom.202102246>.

- [19] U. Ekim, E. İlter, E. Özcan, Y. Temürhan, M. Çelikbilek Ersundu, A.E. Ersundu, Glass-based LED system for indoor horticulture: enhanced plant growth through Sm^{3+} and Tm^{3+} co-doped luminescent glasses, *Physical Chemistry Chemical Physics* 25 (2023) 23150–23163. <https://doi.org/10.1039/D3CP03440B>.
- [20] W. Ye, C. Zhao, X. Shen, C. Ma, Z. Deng, Y. Li, Y. Wang, C. Zuo, Z. Wen, Y. Li, X. Yuan, C. Wang, Y. Cao, High Quantum Yield $\text{Gd}_{4.67}\text{Si}_3\text{O}_{13}:\text{Eu}^{3+}$ Red-Emitting Phosphor for Tunable White Light-Emitting Devices Driven by UV or Blue LED, *ACS Appl Electron Mater* 3 (2021) 1403–1412. <https://doi.org/10.1021/acsaelm.1c00012>.
- [21] Z. Yang, G. Liu, Y. Zhao, Y. Zhou, J. Qiao, M.S. Molokeev, H.C. Swart, Z. Xia, Competitive Site Occupation toward Improved Quantum Efficiency of $\text{SrLaScO}_4:\text{Eu}$ Red Phosphors for Warm White LEDs, *Adv Opt Mater* 10 (2022) 2102373. <https://doi.org/10.1002/adom.202102373>.
- [22] M. Rajendran, S.K. Samal, S. Vaidyanathan, A novel self-activated (bluish-green) and Eu^{3+} doped (red) phosphors for warm white LEDs, *J Alloys Compd* 815 (2020) 152631. <https://doi.org/10.1016/j.jallcom.2019.152631>.
- [23] S. Miao, R. Shi, Y. Zhang, D. Chen, Y. Liang, Deep-Red $\text{Ca}_3\text{Al}_2\text{Ge}_3\text{O}_{12}:\text{Eu}^{3+}$ Garnet Phosphor with Near-Unity Internal Quantum Efficiency and High Thermal Stability for Plant Growth Application, *Adv Mater Technol* 8 (2023) 2202103. <https://doi.org/10.1002/admt.202202103>.
- [24] P. Ling-Hu, X. Guo, J. Hu, C. Deng, R. Cui, Anomalous $^5\text{D}_0 \rightarrow ^7\text{F}_4$ Transition of Eu^{3+} -Doped BaLaGaO_4 Phosphors for WLEDs and Plant Growth Applications, *Adv Opt Mater* 12 (2024) 2301760. <https://doi.org/10.1002/adom.202301760>.
- [25] J. Chen, D. He, W. Wang, S. Li, Z. Zou, J. Liu, Y. Wang, X. Chen, L.-L. Zheng, S. Xie, R. Yu, A double perovskite structure $\text{Ca}_2\text{InTaO}_6:\text{Sm}^{3+}$ orange-red phosphor with high thermal stability for high CRI w-LEDs and plant growth lighting, *J Lumin* 265 (2024) 120252. <https://doi.org/10.1016/j.jlumin.2023.120252>.
- [26] K. Jiang, C. Zhou, W. Li, H. Su, D. He, X. Chen, D. Zhang, S. Xie, R. Yu, A novel highly thermal-stable $\text{Ba}_2\text{GdSbO}_6:\text{Sm}^{3+}$ phosphor with intrinsic deep-red emission for personal identification and plant cultivation LEDs, *J Alloys Compd* 980 (2024) 173518. <https://doi.org/10.1016/j.jallcom.2024.173518>.
- [27] C. Wei, J. Zhang, Z. Sun, J. Ran, S. Li, S. Zhu, C. Jiang, Y. Wen, X. Ran, $\text{Na}_5\text{Y}(\text{MoO}_4)_4:\text{Sm}^{3+}$ red phosphor with good thermal stability and high color rendering index for plant growth lighting and white light emitting diodes, *J Alloys Compd* 991 (2024) 174428. <https://doi.org/10.1016/j.jallcom.2024.174428>.
- [28] Y. Shao, C. Li, Z. Zou, J. Wang, H. Sun, R. Qin, D. Zhang, S. Xie, R. Yu, A high-efficiency double perovskite phosphor $\text{SrLaNaTeO}_6:\text{Mn}^{4+}$: Potential applications in w-LEDs and indoor plant growth lighting, *Ceram Int* 50 (2024) 4433–4445. <https://doi.org/10.1016/j.ceramint.2023.11.161>.

- [29] Q. Bian, H. Wan, L. Wang, S. Ma, S. Li, M. He, G. Zhu, Rare-earth free far-red emitting perovskite phosphor $\text{NaYBa}_4\text{W}_2\text{O}_{12}:\text{Mn}^{4+}$ for indoor plant cultivation lighting, *J Lumin* 265 (2024) 120225. <https://doi.org/10.1016/j.jlumin.2023.120225>.
- [30] Q. Mao, G. Li, X. Shen, J. Xi, L. Pei, X. Li, J. Zhong, Giant enhancement of photoluminescence in Mn^{4+} -activated Ba_2CaWO_6 phosphors via heterovalent doping with rare-earth ions, *Ceram Int* 50 (2024) 6453–6460. <https://doi.org/10.1016/j.ceramint.2023.11.387>.
- [31] B. Li, X. Liu, R. Ma, C. Yang, J. Long, K. Cheng, W. Huang, Far-red emitting $\text{La}_3\text{Li}_5\text{Sb}_2\text{O}_{12}:\text{Mn}^{4+}$ garnet phosphor with superior thermal stability for plant growth application, *Opt Mater* 148 (2024) 114937. <https://doi.org/10.1016/j.optmat.2024.114937>.
- [32] X. Li, Y. Wu, S. Zhang, B. Cai, Y. Gu, J. Song, H. Zeng, CsPbX_3 Quantum Dots for Lighting and Displays: Room-Temperature Synthesis, Photoluminescence Superiorities, Underlying Origins and White Light-Emitting Diodes, *Adv Funct Mater* 26 (2016) 2435–2445. <https://doi.org/10.1002/adfm.201600109>.
- [33] Sixing Li, Yan Pan, Wenming Wang, Yong Li, CsPbX_3 ($X = \text{Cl}, \text{Br}, \text{I}$) perovskite quantum dots embedded in glasses: Recent advances and perspectives, *Chem Eng J* 434 (2022) 134593. <https://doi.org/10.1016/j.cej.2022.134593>.
- [34] C. Liu, W.-T. Huang, R.-S. Liu, Stable glass-protected CsPbX_3 ($X = \text{Cl}, \text{Br}, \text{and I}$) perovskite quantum dots and their applications in backlight LED, *Prog Mater Sci* 143 (2024) 101243. <https://doi.org/10.1016/j.pmatsci.2024.101243>.
- [35] D. Chen, Y. Liu, C. Yang, J. Zhong, S. Zhou, J. Chen, H. Huang, Promoting photoluminescence quantum yields of glass-stabilized CsPbX_3 ($X = \text{Cl}, \text{Br}, \text{I}$) perovskite quantum dots through fluorine doping, *Nanoscale* 11 (2019) 17216–17221. <https://doi.org/10.1039/C9NR07307H>.
- [36] B. Yang, S. Mei, Y. Zhu, D. Yang, H. He, R. Hu, Y. Li, J. Zou, R. Guo, Precipitation promotion of highly emissive and stable CsPbX_3 ($\text{Cl}, \text{Br}, \text{I}$) perovskite quantum dots in borosilicate glass with alkaline earth modification, *Ceram Int* 49, 4 (2023) 6720–6728. <https://doi.org/10.1016/j.ceramint.2022.10.205>.
- [37] M. Guan, Y. Wu, Z. Kuang, Y. Guo, S. Xu, J. Zhang, Mechanical crystallization induced Sm^{3+} -doped CsPbBr_3 quantum dots glass for high-sensitivity temperature sensing, *J Alloys Compd* 965 (2023) 171497. <https://doi.org/10.1016/j.jallcom.2023.171497>.
- [38] B. Yang, Y. Zhu, W. Li, S. Mei, R. Hu, R. Guo, J. Zou, High-efficiency pure-red perovskite quantum dots glass via Dy modification for high quality backlight display, *J Alloys Compd* 1010 (2025) 177437. <https://doi.org/10.1016/j.jallcom.2024.177437>.
- [39] L. Niu, C. Liu, K. Zhang, C. Wang, L. Liu, Y. Chu, J. Ren, J. Zhang, Net Gain at the Near-Infrared from CsPbBr_3 Quantum Dots Sensitized Nd^{3+} -activated Tellurite Glass Under Solar Excitation, *Adv Optical Mater* 12 (2024) 2302953. <https://doi.org/10.1002/adom.202302953>.

- [40] Y.-M. Huang, K.J. Singh, A.-C. Liu, C.-C. Lin, Z. Chen, K. Wang, Y. Lin, Z. Liu, T. Wu, H.-C. Kuo, *Advances in Quantum-Dot-Based Displays*, *Nanomater* 10 (2020) 1327. <https://doi.org/10.3390/nano10071327>.
- [41] S. Mei, J. Yin, Y. Xing, H. He, H. Gu, J. Xia, W. Zhang, C. Liang, G. Xing, R. Guo, Designing high-performance pure-red metal halide perovskite materials and light-emitting diodes for Rec. 2020 display. *Nano Energy* 122 (2024) 109339. <https://doi.org/10.1016/j.nanoen.2024.109339>.
- [42] M. Hao, S. Cheng, Y. He, W. Xiang, N. Ding, W. Xu, C.-G. Ma, X. Liang, Dy³⁺ Doped All-Inorganic Perovskite Nanocrystals Glass toward High-Performance and High-Stability Silicon Photodetectors. *Laser Photonics Rev* 17 (2023) 2200748. <https://doi.org/10.1002/lpor.202200748>.
- [43] Q. He, Y. Zhang, Y. Yu, Y. Chen, M. Jin, E. Mei, X. Liang, L. Zhai, W. Xiang, Ultrastable Gd³⁺ doped CsPbBr₂ nanocrystals red glass for high efficiency WLEDs, *Chem Eng J* 411 (2021) 128530. <https://doi.org/10.1016/j.cej.2021.128530>.
- [44] B. Yang, S. Mei, H. He, Y. Zhu, R. Hu, J. Zou, G. Xing, R. Guo, Lead oxide enables lead volatilization pollution inhibition and phase purity modulation in perovskite quantum dots embedded borosilicate glass, *J Eur Ceram Soc* 42, 1 (2022) 258–265. <https://doi.org/10.1016/j.jeurceramsoc.2021.09.052>.
- [45] Y. Chen, L. Shen, J. Liu, X. Liang, W. Xiang, Eco-friendly Mn-doped CsPbCl₃ perovskite nanocrystal glass with blue-red emission for indoor plant lighting, *J Am Ceram Soc* 104 (2021) 2579–2587. <https://doi.org/10.1111/jace.17644>.
- [46] J. Liu, S. Liu, Y. Chen, Q. Zhao, Y. Zhao, W. Xiang, X. Liang, B. Ren, Sm³⁺-doped CsPbBr₃ NCs glass: A luminescent material for potential use in lighting engineering, *Ceram Int* 45, 17 B (2019) 22688–22693. <https://doi.org/10.1016/j.ceramint.2019.07.304>.
- [47] N. Vahedigharehchopogh, E. Erol, O. Kıbrıslı, A. Genç, M. Çelikkilek Ersundu, A.E. Ersundu, Recyclability of CsPbBr₃ Quantum Dot Glass Nanocomposites for Their Long-Standing Use in White LEDs, *J. Mater. Chem. C* 10 (2022) 16088 – 16099. <https://doi.org/10.1039/D2TC03568E>.
- [48] D. Souri, Z.E. Tahan, A new method for the determination of optical band gap and the nature of optical transitions in semiconductors, *Appl Phys B* 119 (2015) 273–279. <https://doi.org/10.1007/s00340-015-6053-9>.
- [49] M. Kar, T. Körzdörfer, Computational high throughput screening of inorganic cation based halide perovskites for perovskite only tandem solar cells, *Mater Res Express* 7 (2020) 055502. <https://doi.org/10.1088/2053-1591/ab8c0d>.
- [50] N.S. Zailani, M. Fathullah, Sm³⁺ as potential co-dopant candidate in scheelite molybdate/tungstate red phosphor: A review, *AIP Conf. Proc.* 1835,1 (2017) 020044. <https://doi.org/10.1063/1.4981866>.

- [51] S.M. Shim, C. Liu, Y.K. Kwon, J. Heo, Lead Sulfide Quantum Dots Formation in Glasses Controlled by Erbium Ions. *J Am Ceram Soc* 93 (2010) 3092–3094. <https://doi.org/10.1111/j.1551-2916.2010.04045.x>.
- [52] R. Rajaramakrishna, B. Knorr, V. Dierolf, R.V. Anavekar, H. Jain, Spectroscopic properties of Sm³⁺-doped lanthanum borogermanate glass, *J Lumin* 156 (2014) 192–198. <https://doi.org/10.1016/j.jlumin.2014.07.021>.
- [53] O. Kıbrıslı, A.E. Ersundu, M. Çelikkilek Ersundu, Dy³⁺ doped tellurite glasses for solid-state lighting: An investigation through physical, thermal, structural and optical spectroscopy studies, *J Non-Cryst Solids* 513 (2019) 125–136. <https://doi.org/10.1016/j.jnoncrysol.2019.03.020>.
- [54] X. Li, X. Deng, J. Hong, J. Lin, J. Lv, M. Yu, X. Guan, S. Du, Y. Yu, D. Chen, Color adjustable CsPbX₃ (X=Cl, Br, I) perovskite quantum dots germanate glass, *J Lumin* 266 (2024) 120256. <https://doi.org/10.1016/j.jlumin.2023.120256>.
- [55] J.-S. Yao, J. Ge, B.-N. Han, K.-H. Wang, H.-B. Yao, H.-L. Yu, J.-H. Li, B.-S. Zhu, J.-Z. Song, C. Chen, Q. Zhang, H.-B. Zeng, Y. Luo, S.-H. Yu, Ce³⁺-Doping to Modulate Photoluminescence Kinetics for Efficient CsPbBr₃ Nanocrystals Based Light-Emitting Diodes, *J Am Chem Soc* 140 (2018) 3626–3634. <https://doi.org/10.1021/jacs.7b11955>.
- [56] L. Niu, L. Wang, W. Li, S. Qian, L. Liu, C. Wang, J. Ren, J. Zhang, Enhanced luminescence and high stability in Gd³⁺-doped CsPbBr₃ perovskite quantum dots glasses for X-ray detection, *Ceram Int* 50, 1 A (2024) 1303–1308. <https://doi.org/10.1016/j.ceramint.2023.10.202>.
- [57] J. Wang, C. Liu, G. Zhang, J. Xie, J. Han, X. Zhao, Crystallization properties of magnesium aluminosilicate glass-ceramics with and without rare-earth oxides, *J Non-Cryst Solids* 419 (2015) 1–5. <https://doi.org/10.1016/j.jnoncrysol.2015.01.024>.
- [58] Y. Zhu, J. Zhu, H. Song, J. Huang, Z. Lu, G. Pan, Samarium doping improves luminescence efficiency of Cs₃Bi₂Br₉ perovskite quantum dots enabling efficient white light-emitting diodes, *J Rare Earths* 39 (2021) 374–379. <https://doi.org/10.1016/j.jre.2020.06.007>.
- [59] Y. Zhang, J. Liu, H. Zhang, Q. He, X. Liang, W. Xiang, Ultra-stable Tb³⁺:CsPbI₃ nanocrystal glasses for wide-range high-sensitivity optical temperature sensing, *J Eur Ceram Soc* 40 (2020) 6023–6030. <https://doi.org/10.1016/j.jeurceramsoc.2020.07.016>.
- [60] Q. Dong, J. Yang, J. Cui, F. Xu, F. Yang, J. Peng, F. Du, X. Ye, S. Yang, A narrow-band ultra-bright green phosphor for LED-based applications, *Dalton Trans* 49 (2020) 1935–1946. <https://doi.org/10.1039/C9DT04092G>.
- [61] Q. Dong, P. Xiong, J. Yang, Y. Fu, W. Chen, F. Yang, Z. Ma, M. Peng, Bismuth activated blue phosphor with high absorption efficiency for white LEDs, *J Alloys Compd* 885 (2021) 160960. <https://doi.org/10.1016/j.jallcom.2021.160960>.

- [62] J. Deng, H. Zhang, X. Zhang, Y. Zheng, J. Yuan, H. Liu, Y. Liu, B. Lei, J. Qiu, Ultrastable red-emitting phosphor-in-glass for superior high-power artificial plant growth LEDs, *J Mater Chem C* 6 (2018) 1738–1745. <https://doi.org/10.1039/C7TC05250B>.
- [63] J. Liu, L. Shen, Y. Chen, Y. Zhao, Y. Zhang, M. Jin, H. Yang, Y. Zhang, W. Xiang, X. Liang, Highly luminescent and ultrastable cesium lead halide perovskite nanocrystal glass for plant-growth lighting engineering, *J Mater Chem C* 7 (2019) 13606–13612. <https://doi.org/10.1039/C9TC04799A>.
- [64] Z. Zhang, L. Shen, H. Zhang, L. Ding, G. Shao, X. Liang, W. Xiang, Novel red-emitting CsPb_{1-x}Ti_xI₃ perovskite QDs@glasses with ambient stability for high efficiency white LEDs and plant growth LEDs, *Chem Eng J* 378 (2019) 122125. <https://doi.org/10.1016/j.cej.2019.122125>.
- [65] Z. Zhang, L. Shen, Y. Zhao, Y. Zhang, H. Yang, W. Xiang, X. Liang, G. Chen, H. Yu, Coexisting CsPbCl₃:CsPbI₃ perovskite nanocrystal glasses with high luminescence and stability, *Chem Eng J* 385 (2020) 123415. <https://doi.org/10.1016/j.cej.2019.123415>.
- [66] W. Chen, X. Zhang, J. Zhou, H. Zhang, J. Zhuang, Z. Xia, Y. Liu, M.S. Molokeev, G. Xie, B. Lei, Glass-ceramics with thermally stable blue-red emission for high-power horticultural LED applications, *J Mater Chem C* 8 (2020) 3996–4002. <https://doi.org/10.1039/D0TC00061B>.
- [67] Z. Xu, J. Xia, Y. Yang, D. Chen, X. Liu, J. Qiu, Z. Li, Modulation of optical properties for lighting applications based on CsPbBr_{3-x}I_x quantum dot doped glasses, *J Eur Ceram Soc* 44 (2024) 3226–3235. <https://doi.org/10.1016/j.jeurceramsoc.2023.12.064>.
- [68] Q. Huang, M. He, Y. Yang, N. Lai, Q. Zhang, Y. Quan, J. Liao, Y. Yang, C. Wang, J. Yang, T. Sun, R. Wang, Moisture-Stable CsSnBr₃ Quantum Dots and SnO₂ Glass-Ceramics for Broadband White-Emitting Diodes, *ACS Appl Nano Mater* 7 (2024) 17967–17977. <https://doi.org/10.1021/acsanm.4c03202>.